

# Developing Flying Explorer for Autonomous Digital Modelling in Wild Unknowns

Naizhong Zhang<sup>1,\*,#</sup>, Yaoqiang Pan<sup>2,\*</sup>, Yangwen Jin<sup>2,\*</sup>, Peiqi Jin<sup>2</sup>, Kewei Hu<sup>2</sup>,  
Xiao Huang<sup>1</sup>, and Hanwen Kang<sup>2,#</sup>

**Abstract**—This work presents an innovative solution for robotic odometry, path planning and exploration in wild unknown environments, focusing on digital modelling. The approach uses a minimum cost formulation with pseudo-randomly generated objectives, integrating multi-path planning and evaluation, with emphasis on full coverage of unknown maps based on feasible boundaries of interest. The evaluation carried out on a robotic platform with a lightweight 3D LiDAR sensor model, assesses the consistency and efficiency in exploring completely unknown subterranean-like areas. The algorithm allows for dynamic changes to the desired target and behaviour. At the same time, the paper details the design of AREX, highlighting its robust localisation, mapping and efficient exploration target selection capabilities, with a focus on continuity in exploration direction for increased efficiency and reduced odometry errors. The real-time, high-precision environmental perception module is identified as critical for accurate obstacle avoidance and exploration boundary identification.

## I. INTRODUCTION

The Digital Twin (DT) concept, introduced by NASA in 1991, involves virtual representations of physical assets that reflect their context through data from various sensors[1]. Digital modelling (DM) is a critical task within the DT framework[2], contributing to insights, predictions and performance optimisation in industries such as manufacturing and transportation. Industries that rely on digital models, such as agriculture and construction, benefit greatly from drones with exceptional obstacle-avoidance capabilities[3]. These drones can generate 3D models of complex terrains and intricate plantations. The introduction of digital models in plantations significantly enhances daily tasks like harvest planning, and revolutionizing orchard management[4], [5].

This article explores a unique mapping and exploration theory that paves the way for autonomous, drone-based, rapid exploration models of orchards. In the field of management, the development of autonomous robotic platforms with exploration and mapping capabilities is revolutionary[6]. Robots, especially those equipped with 3D LiDAR sensors, contribute essential elements to DM, including accurate 3D modelling[7]. Their ability to mark characteristic points at specific locations is proving beneficial for later data collection and processing[8], [9].

Exploring and mapping unknown and unstructured environments has always been an important and fundamental task for robots. This includes tasks such as inspecting large infrastructures, surveying buildings, performing search and rescue missions, and exploring underground spaces. The exploration of wild, unknown and unstructured environments, especially those that are harsh and lack GPS connectivity, has become a major focus for autonomous robotic exploration missions. This focus has grown significantly in recent years, particularly with events such as the DARPA Subterranean Challenge. In this challenge, teams of robots are tasked with exploring and identifying artefacts in complex and unstructured environments. In conjunction with Simultaneous Localisation and Mapping (SLAM), overcoming the challenges of motion planning and exploration behaviour is one of the most fundamental issues in these diverse applications.



Fig. 1: AREX: Flight System Designed for High Durability, Multi-Scenario Exploration, and Environmental Modeling.

Robotic localisation, path planning, and exploration are fundamental research areas for building such a robotic system[10], with various solutions to the challenge of fully exploring unknown areas, including pattern-based approaches, frontier methods and entropy-based strategies[11]. Occupancy-based path planning, which relies on maps of occupied and free space, often uses algorithms such as Dijkstra's or advanced versions of A\* and jump-point-search. Alternatively, the Rapidly-Exploring Random Tree (RRT) algorithm, in its modern versions, serves as a core component of some path planning solutions, offering computational efficiency and flexibility, but lacking the guarantee of finding the shortest path within

\* Contribute Equally

# Correspond Authors

<sup>1</sup> N. Zhang, X. Huang are with the College of Civil Aviation, Nanjing University of Aeronautics and Astronautics, Nanjing, China

<sup>2</sup> Y.Pan, Y.Jin, P.Jin, K.Hu and H.Kang are with the College of Engineering, South China Agriculture University, Guangzhou, China

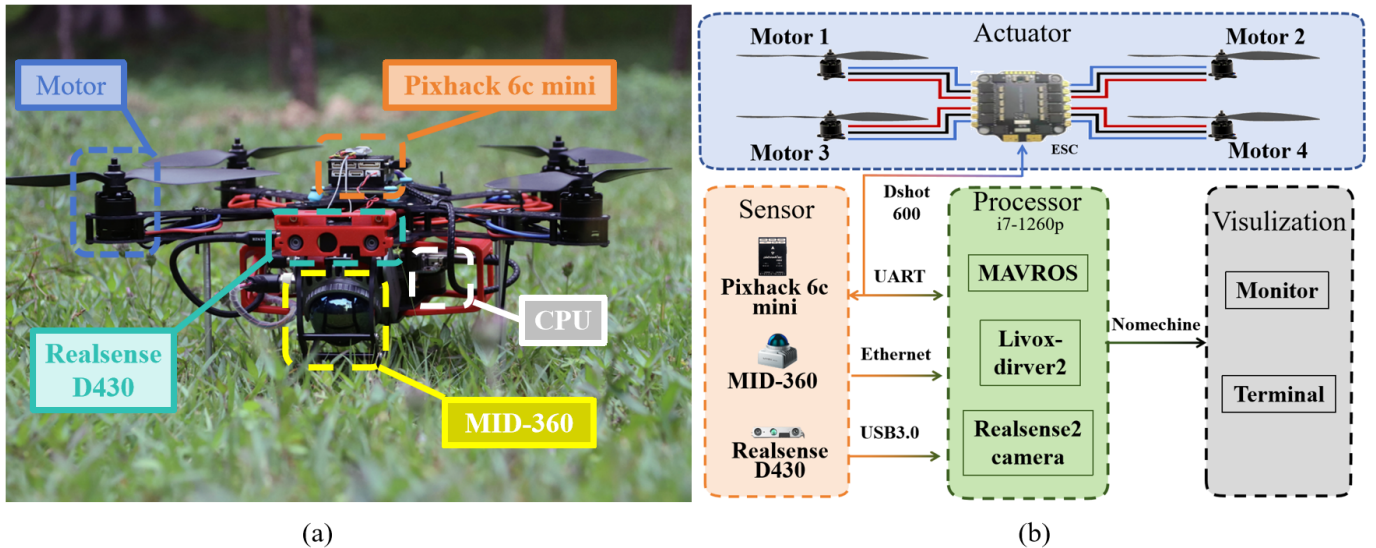


Fig. 2: Robot Design (a) AREX’s frame structure and sensor layout. The MID-360 LiDAR is positioned at the front of the fuselage at a 45° angle to the horizontal z-axis, while the Realsense D430 is mounted above the MID-360 to fill in blind spots in the point cloud. The front dual arms of AREX form a 120° angle, maximizing the avoidance of obstructing the LIDAR’s scanning range. (b) AREX’s circuitry structure. Reflects the circuitry between the ESCs and motors, as well as the communication interfaces and protocols among various modules.

a limited number of iterations. Traditionally, exploration and planning problems have been treated separately. For example, in [12], a deep reinforcement model selects optimal bounds and an A\* algorithm finds the shortest path. In [13], stochastic differential equations identify optimal bounds and an RRT\* path planner computes the path. Recently, the integration of exploration into the central planning problem has gained attention, with solutions such as Next-Best-View planners [14] being foundational. Exploration RRT (ERRT)[15] shares core concepts with Next-Best-View planners but is innovative in its algorithmic implementation. ERRT explicitly solves paths to pseudo-random objectives, which distinguishes it from the iterative evaluation of RRT branches. In particular, ERRT computes optimal actuation for trajectory following through a receding horizon NMPC problem, with the proposed method using the Optimization Engine, an open-source Rust-based optimization software.

This work presents a novel solution to the combined challenge of robotic odometry, path planning, and exploration for digital modelling in wild unknown environments. It employs a minimum cost formulation with pseudo-randomly generated objectives, integrating multi-path planning and evaluation. This evaluation considers information gain and total distance. Our approach emphasises full coverage of the unknown map, depending on the availability of feasible boundaries of interest. The evaluation focuses on a robotic platform with a lightweight 3D LiDAR sensor model and evaluates the consistency and efficiency of exploring a completely unknown subterranean-like and unstructured area. The algorithm is designed with versatile robot localisation and motion planning that allows dynamic changes to the desired goal and behaviour. Our detailed contributions are presented below.

- Developing the Aerial Robot EXploration (AREX) sys-

tem, including its hardware and software framework, for autonomous digital modelling in unstructured and unknown environments.

- Developing a novel algorithm for autonomous exploration in unknown environments for multiple scenarios.
- Demonstration of the developed AREX system in real-world applications, showcases its effectiveness in several scenarios.

The rest of this paper is organised as follows. Section II will overview the system setup and methodologies, followed by the experimental results and discussions given in Sections III. Then the conclusions are given in Section IV.

## II. METHODOLOGIES

### A. Robot Design

1) *Hardware Design:* AREX features a frame design that prioritises strength, durability and ease of assembly. Rigid bodywork is made from carbon fibre with a density of  $0.00153 \text{ mm}^3/g$ , resulting in a lightweight 250g frame. The diagonal engine wheelbase is 380mm, powered by a 4s 30C 4000mah battery. The platform features four SUNNYSKY X-2216 II KV880 brushless DC motors with APC 9045 two-blade propellers, controlled by an XF 35A 4in1 electronic speed controller. For autopilot functions, the Pixhack 6c mini provides attitude and thrust control. The AREX measures 500x500x220mm, weighs 1.9kg and has an endurance of 10 minutes.

The schematic in Fig.2(b) illustrates AREX’s configuration. The Pixhack 6c Mini Flight Controller communicates with the 4in1 Electronic Speed Controller (ESC) using the Dshot600 protocol, while also connecting to the on-board computer via a UART. This allows IMU data to be received from the

onboard computer and desired attitude and throttle commands to be received from the flight plan. The sensor setup, shown in Fig.2, includes a LIVOX MID-360 mixed LiDAR with a 360° horizontal and 59° vertical field of view. At the front, a RealSense D430 depth camera operates at 10Hz for the LiDAR and 30Hz for the camera. The Pixhack flight controller outputs 9-axis IMU data at 200Hz.

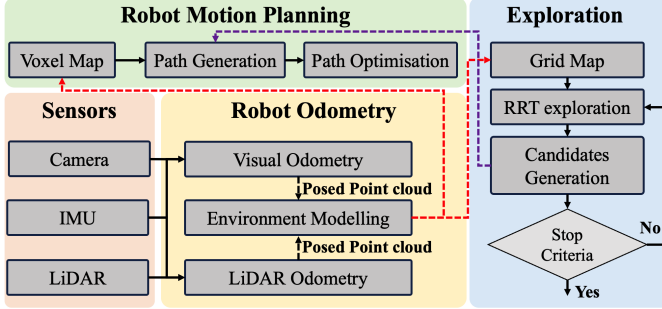


Fig. 3: AREX: Flight System Designed for High Durability, Multi-Scenario Exploration, and Environmental Modeling.

2) *Software Design*: The software architecture of AREX, shown in Fig.3, consists of several key modules. In the Robot Odometry module, data from LiDAR odometry or visual odometry is used to estimate the 6-axis Degree of Freedom (DOF) positional attitude of AREX. The resulting position and point cloud data are used in the exploration module to maintain an octomap representing the exploration state of the environment. This module uses RRT to identify a series of boundary points in the unknown region of the Octomap. The directional RRT exploration proposed in this paper determines the final exploration target point. This information is then fed into the motion planning module which, using a PD controller, calculates the desired attitude and throttle for AREX based on the path points. Finally, the calculated commands are sent to the flight controller. In cases where the stop strategy is triggered, AREX returns autonomously to the starting point and lands or remains in place.

### B. Robot odometry

1) *Visual odometry*: VINS-Fusion[16] is used for visual odometry, and the loss function is constructed in the formula below:

$$\min_{\mathcal{X}} \left\{ \underbrace{\|\mathbf{r}_p - \mathbf{H}_p \mathcal{X}\|^2}_{\text{prior factor}} + \underbrace{\sum_{k \in \mathcal{B}} \|\mathbf{r}_B(\hat{\mathbf{z}}_{b_{k+1}}^{b_k}, \mathcal{X})\|_{\mathbf{P}_{b_{k+1}}}^2}_{\text{IMU propagation factor}} + \underbrace{\sum_{(l,j) \in \mathcal{C}} \rho(\|\mathbf{r}_l(\hat{\mathbf{z}}_l^{c_j}, \mathcal{X})\|_{\mathbf{P}_l^{c_j}}^2)}_{\text{vision factor}} \right\} \quad (1)$$

where the first item is the priority after the marginalization, the second item is the IMU residual, and the third item is the

visual residual. Because of the complex design, this system is very robust. So we combine it with improved FAST-LIO for better odometry. A graph is shown in Fig. 4 to illustrate the framework of VINS-Fusion.

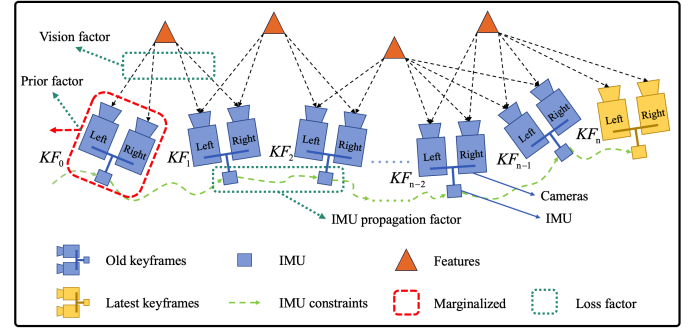


Fig. 4: A graphic illustration of the VINS-Fusion framework. If the latest keyframe comes, it will be kept, and the visual and IMU measurements of the oldest frame will be marginalized. The prior factor of the loss function is obtained from marginalization. We can get the IMU propagation factor from IMU pre-integration. By computing the reprojection error between two keyframes, we can get the vision factor.

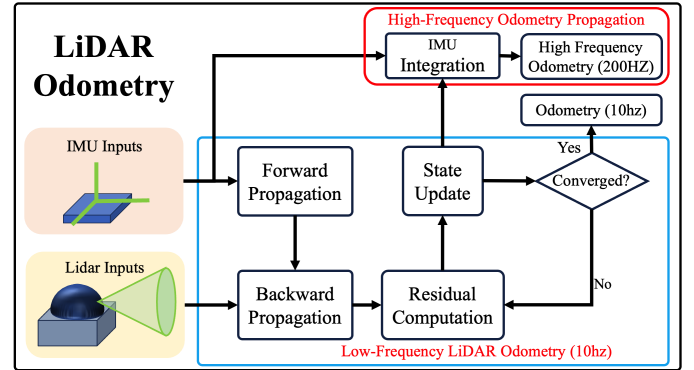


Fig. 5: System overview of improved FAST-LIO, which can output high-frequency odometry.

2) *LiDAR odometry*: FAST-LIO[17] is used for LiDAR odometry, error-state iterated Kalman filter (ESIKF) is used to update the state of the system. The overview of improved FAST-LIO is shown in Fig. 5. The linearized update formula of the error-state variables in FAST-LIO is

$$\tilde{\mathbf{x}}_{i+1} \simeq \mathbf{F}_{\tilde{\mathbf{x}}} \tilde{\mathbf{x}}_i + \mathbf{F}_{\mathbf{w}} \mathbf{w}_i \quad (2)$$

where the matrix  $\mathbf{F}_{\tilde{\mathbf{x}}}$  and  $\mathbf{F}_{\mathbf{w}}$  in (2) is computed in (3).

We can get new state variables through forward propagation, which is used to compensate for the motion distortion of the LiDAR in backward propagation, the calculation formula is shown below:

$${}^{L_k} \mathbf{p}_{f_j} = {}^I \mathbf{T}_L^{-1} I_k \tilde{\mathbf{T}}_{I_j} {}^I \mathbf{T}_L^{L_j} \mathbf{p}_{f_j} \quad (4)$$

This LIO algorithm can quickly and robustly output LiDAR odometry, but the frequency of the odometry it outputs is only 10hz, which is too low for robots that need to obtain pose information in real-time. A high-frequency LiDAR inertial

$$\begin{aligned}
 \mathbf{F}_{\bar{x}} &= \begin{pmatrix} \text{Exp}(-(\omega_m - \hat{\mathbf{b}}_\omega)\Delta t) & 0 & 0 & -\mathbf{A}((\omega_m - \hat{\mathbf{b}}_\omega)\Delta t)^T \Delta t & 0 & 0 \\ 0 & \mathbf{I} & \mathbf{I}\Delta t & 0 & 0 & 0 \\ -{}^G\hat{\mathbf{R}}_{I_i}(\mathbf{a}_m - \hat{\mathbf{b}}_a)^T \Delta t & 0 & \mathbf{I} & 0 & -{}^G\hat{\mathbf{R}}_{I_i}\Delta t & \mathbf{I}\Delta t \\ 0 & 0 & 0 & \mathbf{I} & 0 & 0 \\ 0 & 0 & 0 & 0 & \mathbf{I} & 0 \\ 0 & 0 & 0 & 0 & 0 & \mathbf{I} \end{pmatrix} \\
 &\approx \begin{pmatrix} \mathbf{I} & 0 & 0 & \mathbf{I}\Delta t & 0 & 0 \\ 0 & \mathbf{I} & \mathbf{I}\Delta t & 0 & 0 & 0 \\ -{}^G\hat{\mathbf{R}}_{I_i}(\mathbf{a}_m - \hat{\mathbf{b}}_a)^T \Delta t & 0 & \mathbf{I} & 0 & -{}^G\hat{\mathbf{R}}_{I_i}\Delta t & \mathbf{I}\Delta t \\ 0 & 0 & 0 & \mathbf{I} & 0 & 0 \\ 0 & 0 & 0 & 0 & \mathbf{I} & 0 \\ 0 & 0 & 0 & 0 & 0 & \mathbf{I} \end{pmatrix} \\
 \mathbf{F}_w &= \begin{pmatrix} -\mathbf{A}((\omega_m - \hat{\mathbf{b}}_\omega)\Delta t)^T \Delta t & 0 & 0 & 0 \\ 0 & 0 & 0 & 0 \\ 0 & -{}^G\hat{\mathbf{R}}_{I_i}\Delta t & 0 & 0 \\ 0 & 0 & \mathbf{I}\Delta t & 0 \\ 0 & 0 & 0 & \mathbf{I}\Delta t \\ 0 & 0 & 0 & 0 \end{pmatrix} \\
 &\approx \begin{pmatrix} -\mathbf{I}^T \Delta t & 0 & 0 & 0 \\ 0 & 0 & 0 & 0 \\ 0 & -{}^G\hat{\mathbf{R}}_{I_i}\Delta t & 0 & 0 \\ 0 & 0 & \mathbf{I}\Delta t & 0 \\ 0 & 0 & 0 & \mathbf{I}\Delta t \\ 0 & 0 & 0 & 0 \end{pmatrix}
 \end{aligned} \tag{3}$$

odometer is used here to achieve the frequency required by robot, whose frequency of odometry can reach 200hz. Whenever the ESKF is updated with a frame of odometry, this odometry will be recorded, and the newly incoming IMU measurement data will be integrated based on this optimized odometry. The calculation is shown in the following formulas. When a new frame of IMU data  $\mathbf{a}_m$  arrives:

$$\mathbf{a}_c = -\frac{\mathbf{a}_m}{\|\mathbf{a}_m\|} \cdot G_m \tag{5}$$

where  $\mathbf{a}_m$  represents the acceleration measurement of IMU,  $\mathbf{a}_c$  represents the input acceleration of current time,  $G_m$  represents the preset gravity constant, which is a scalar.

Since we record the optimized pose output by the system, we have:

$$\mathbf{a}_0 = \mathbf{R}_i(\mathbf{a}_p - \mathbf{b}_a) - \mathbf{g} \tag{6}$$

where  $\mathbf{a}_p$  represents the input acceleration of previous time,  $\mathbf{R}_i$  is the previous pose,  $\mathbf{b}_a$  is the bias of acceleration,  $\mathbf{g}$  is the estimated gravity in odometry of FAST-LIO. Then using median angular velocity to update the rotation matrix:

$$\begin{aligned}
 \boldsymbol{\omega} &= \frac{\boldsymbol{\omega}_0 + \boldsymbol{\omega}_1}{2} \\
 \mathbf{R}_{i+1} &= \mathbf{R}_i \text{Exp}(\boldsymbol{\omega}\Delta t)
 \end{aligned} \tag{7}$$

where  $\boldsymbol{\omega}_0$  is the previous angular velocity measurement of IMU,  $\boldsymbol{\omega}_1$  is the current angular velocity measurement of IMU. Then transfer the acceleration to the world coordinate and calculate the median value:

$$\mathbf{a} = \frac{\mathbf{a}_0 + \mathbf{a}_1}{2} \tag{8}$$

Then the position and linear velocity can be updated as follows:

$$\begin{aligned}
 \mathbf{p}_{i+1} &= \mathbf{p}_i + \mathbf{v}_i\Delta t + \frac{1}{2}\mathbf{a}\Delta t^2 \\
 \mathbf{v}_{i+1} &= \mathbf{v}_i + \mathbf{a}\Delta t
 \end{aligned} \tag{9}$$

### C. Robot motion planning

1) *Environment Representation*: The motion planning map is a localised raster map composed of radar point cloud frames represented by a one-dimensional array. The value of each array element indicates the occupancy state of the corresponding grid, with 0 for free space and 1 for obstacles. The map has default dimensions of  $L, W, H$  and a grid size of  $size_{grid}$ , resulting in an array size of  $array\_size$ . The calculation for  $array\_size$  is given by

$$array\_size = \frac{L \cdot W \cdot H}{size_{grid}^3} \tag{10}$$

The index value of each grid can be obtained by the Eq.11

$$Id_i = h_i \cdot num_w \cdot num_l + w_i \cdot num_l + l_i \tag{11}$$

where  $h_i, w_i, l_i$  represent the indices of layers in three directions of  $grid_i$ ,  $num_w$  denotes the number of grids in the width direction, and  $num_l$  is similar to  $num_w$ .

On receipt of a point cloud frame, the 2D array values representing local map obstacle locations are set to zero. Each spatial point in the point cloud frame calculates the corresponding index value and assigns the value 1 to the corresponding position in the array. Spatial points outside the specified map area are discarded. The layer indexes of the raster in which the spatial points are located are as follows:

$$\begin{aligned}
 w_i &= \lfloor \frac{P_i \cdot x}{size_{grid}} \rfloor + \frac{num_w}{2} \\
 l_i &= \lfloor \frac{P_i \cdot y}{size_{grid}} \rfloor + \frac{num_l}{2} \\
 h_i &= \lfloor \frac{P_i \cdot z}{size_{grid}} \rfloor + \frac{num_h}{2}
 \end{aligned} \tag{12}$$

To improve the feasibility of the motion planning path, obstacles are expanded by applying a preset expansion coefficient to each point in the point cloud frame, generating an expanded point set. The corresponding array positions are then assigned a value of 1 based on the spatial locations of the points in this set. The point set expression formula is as follows:

$$\begin{aligned} & [(P_i \cdot x - \lambda_{inflat}) + size_{grid} \cdot a, \\ & (P_i \cdot y - \lambda_{inflat}) + size_{grid} \cdot b, \\ & (P_i \cdot z - \lambda_{inflat}) + size_{grid} \cdot c]^T \\ & a, b, c \in [0, n_{step}] \\ & n_{step} = \lceil \frac{\lambda_{inflat}}{size_{grid}} \rceil \end{aligned} \quad (13)$$

2) *Local Motion Planner*: Our work follows EGO-planner [18], a optimization-based framework for robot motion planning.

**Collision-Free Trajectory Generation**: By given a motion goal, the motion planning module generates an initial B-spline path  $\Phi$  that does not take collisions into account. The start and end points of the path are the robot's position and the goal, respectively. Then the control point  $Q_i$ , which exists in the obstacle, finds the anchor point  $p_i$  at the obstacle surface for the control point that exists inside the obstacle. Then the obstacle distance from  $Q_i$  to the obstacle is defined as

$$d_i = (\mathbf{Q}_i - \mathbf{p}_{ij}) \cdot \mathbf{v}_i \quad (14)$$

A collision-free path is obtained by optimizing the position of  $Q_i$  such that  $d_i > 0$ .

**Gradient-based Trajectory Optimization**: The cost function of the trajectory optimization is:

$$\min J = \lambda_s J_s + \lambda_c J_c + \lambda_d J_d, \quad (15)$$

where  $J_s$  is the smoothness penalty,  $J_c$  is for collision, and  $J_d$  indicates feasibility.  $\lambda_s, \lambda_c, \lambda_d$  are weights for each penalty terms. We use a uniform B-spline, which means that for each control point  $\mathbf{Q}_i \in \mathbb{R}^3$ , they have the same time interval from the latter control point, i.e.  $\Delta t = t_{i+1} - t_i$ . Thus the velocity  $\mathbf{V}_i$ , acceleration  $\mathbf{A}_i$ , and jerk  $\mathbf{J}_i$  at each control point are obtained by

$$\mathbf{V}_i = \frac{\mathbf{Q}_{i+1} - \mathbf{Q}_i}{\Delta t}, \mathbf{A}_i = \frac{\mathbf{V}_{i+1} - \mathbf{V}_i}{\Delta t}, \mathbf{J}_i = \frac{\mathbf{A}_{i+1} - \mathbf{A}_i}{\Delta t}. \quad (16)$$

For the smoothing term penalty, we examine the squares of the second-order and third-order derivatives of the control points concerning  $\Delta t$  each. The second and third-order derivatives of the B-spline curve are reduced by minimizing the second and third-order derivatives of the control points for the node vector  $\Delta t$  using the convex envelope property of the B-spline. This smoothness penalty is defined as follows, considering a total of  $n$  control points on the B-spline:

$$J_s = \sum_{i=1}^{n-1} \|\mathbf{A}_i\|^2 + \sum_{i=1}^{n-2} \|\mathbf{J}_i\|^2 \quad (17)$$

For the collision penalty, we set a safe distance  $S_f$  and satisfy  $d_i < d_s$  by the penalty requirement function. The collision penalty function is as follows:

$$j_c(i) = \begin{cases} 0 & (c_i \leq 0) \\ c_i^3 & (0 < c_i \leq s_f) \\ 3s_f c_i^2 - 3s_f^2 c_i + s_f^3 & (c_i > s_f) \end{cases} \quad (18)$$

where  $c_i = s_f - d_i$ ,

where  $d_{ij}$  comes from the Eq.14. Hence, the total collision penalties across the entire path result from the summation of penalties associated with individual control points  $\mathbf{Q}_i$ . The formula can be expressed as follows:

$$J_c = \sum_{i=1}^n j_c(\mathbf{Q}_i). \quad (19)$$

To guarantee feasibility in the context of the Feasibility penalty, higher-order derivatives of each control in the x, y, and z dimensions are constrained to values below a predefined kinetic limit. The penalty function is articulated as follows:

$$J_d = \sum_{i=1}^n w_v F(\mathbf{V}_i) + \sum_{i=1}^{n-1} w_a F(\mathbf{A}_i) + \sum_{i=1}^{n-2} w_j F(\mathbf{J}_i) \quad (20)$$

$w_v, w_a$ , and  $w_j$  represent the weights assigned to different higher-order derivatives for each control point. Meanwhile, the definition of  $F(\cdot)$  is as follows:

$$F(\mathbf{C}) = \sum_{r=x,y,z} f(c_r) \quad (21)$$

$$f(c_r) = \begin{cases} a_1 c_r^2 + b_1 c_r + c_1 & (c_r \leq -c_j) \\ (-\lambda c_m - c_r)^3 & (-c_j < c_r < -\lambda c_m) \\ 0 & (-\lambda c_m \leq c_r \leq \lambda c_m) \\ (c_r - \lambda c_m)^3 & (\lambda c_m < c_r < c_j) \\ a_2 c_r^2 + b_2 c_r + c_2 & (c_r \geq c_j) \end{cases} \quad (22)$$

where  $c_r \in \mathbf{C} \in \{\mathbf{V}_i, \mathbf{A}_i, \mathbf{J}_i\}$ ,  $a_1, b_1, c_1, a_2, b_2, c_2$  satisfy second-order continuity.  $c_m$  is the derivative limit, and  $c_j$  represents the intersection points between the quadratic and cubic intervals. For a given condition where  $\lambda < 1 - \epsilon$  and  $\epsilon \ll 1$ , the objective is to ensure the structure adheres to the imposed constraint.

## D. Robot Exploration Module

1) *Environmental Modelling*: By maintaining the collection of undistorted LiDAR feature points, a high-precision global point cloud map is composed. This process is outlined by Eq. 23.  ${}^{Lk}\mathbf{p}_{f_j}$  represents the undistorted LiDAR feature points in the LiDAR coordinate obtained through 4,  ${}^I\mathbf{T}_L$  denotes the transformation relationship from the LiDAR coordinate to the IMU coordinate, and  ${}^G\mathbf{T}_{I_k}$  signifies the system state corresponding to the LiDAR frame.

$${}^G\bar{\mathbf{p}}_{f_j} = {}^G\bar{\mathbf{T}}_{I_k} {}^I\mathbf{T}_L {}^{Lk}\mathbf{p}_{f_j}; j = 1, \dots, m. \quad (23)$$

A 2D occupancy map is constructed to represent the known and unknown regions in the scene, where each raster has only

three values: -1, 0, and 1 for the unknown, idle, and occupied states, respectively. When using the RRT-based boundary point detector, by querying whether the grid on the tree growth line is the unknown state value -1, we can determine whether to find the boundary point of the unknown region.

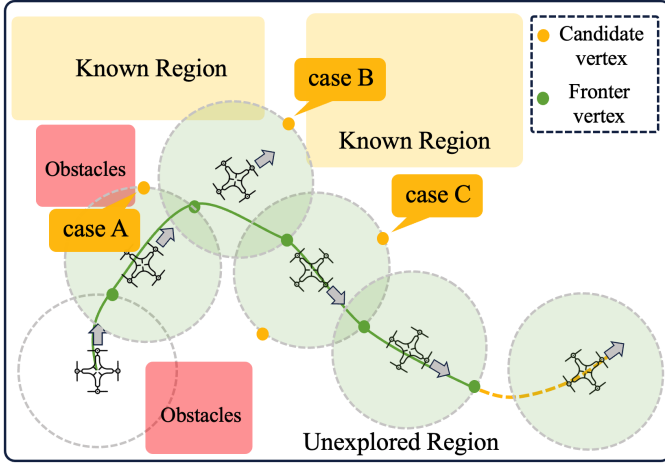


Fig. 6: Demonstration of RRT exploration strategy, case A: Candidate vertices close to an obstacle will not be considered, case B: Candidate vertices close to a known area will not be considered, case C: Candidate vertex far away from the exploration direction will not be considered.

The occupancy state of the occupied map is updated by LiDAR point cloud frames in global coordinates, and we select the point clouds with height values of 0-2m in the point cloud frames in global coordinates to represent the state of the raster. A grid is considered occupied when a point cloud exists in the grid, while a grid is considered idle when the occupied grid is connected to the robot's position and the line passes through it. As the Explorer moves, the LiDAR point cloud frames change with the environment, and the occupancy map is updated by aggregating the odometer information.

2) *Direction-Aware RRT Exploration*: Algorithm 1 demonstrates the Direction-Aware exploration based on RRT. The following are the relevant definitions:

- **R** represents the data frames from the LiDAR.
- **O** represents the odometry information.
- **M** represents the grid map.
- **CGs** represents the frontier points.
- **T<sub>t</sub>** represents the expected exploration goal at time t.
- **P<sub>s</sub>** represents the smoothed path.
- **E<sub>x</sub>** represents the flag for executing exploration

The four key nodes shown in Alg.1 are described below:

- **OctomapServer**: accepts radar data frame information and odometer information for constructing a 2D occupancy map representing the scene exploration.
- **FrontierDetector**: accepts the 2D occupancy map and odometer information constructed by Octomap Server and searches for boundary points of unexplored environment by RRT and outputs a list of candidate target points.
- **RevenueCalculator**: accepts the 2D occupancy map, odometer information, and candidate target points, calculates the value of the utility function of the candidate

target points, and outputs the target point with the highest score.

- **PathPlanner**: accepts target points, radar data frames, and odometer information to plan a collision-free smooth path for the robot.

---

**Algorithm 1:** Direction-Aware RRT exploration
 

---

**Data:** **R**, **O**, **E<sub>x</sub>**  $\leftarrow$  True

**Result:** High-quality point cloud map

**while** **E<sub>x</sub>** = True **do**

**M**  $\leftarrow$  Octomap\_Server(**R**, **O**);

**CGs**  $\leftarrow$  Frontier\_Detector(**M**, **O**);

**if** **CGs**  $\neq$   $\emptyset$  **then**

**T<sub>t</sub>**  $\leftarrow$  Revenue\_Calculator(**CGs**, **O**, **M**);

**P<sub>s</sub>**  $\leftarrow$  Path\_Planner(**T**, **O**);

**else**

**E<sub>x</sub>**  $\leftarrow$  False

**end**

**end**

---

3) *Evaluation Strategy*: The exploration strategy in this work evaluates candidate observation positions to find the optimal frontier vertex. This strategic approach aims to shorten the exploration time, reduce the overall step size, and ultimately increase efficiency. Our strategy takes into account three key factors: the distance of the robot to the observation position, the expected information gain, and the correlation with the direction of the last exploration target. Fig.6 visually demonstrates our exploration strategy.

$$R(CG_i) = \lambda_I \cdot f_i^I - \lambda_N \cdot f_i^N \quad (24)$$

$$CG_i = \text{Arg} \max_{CG_i \in CGs} (R(CG_i))$$

In the explored method[19], the robot chooses the nearest, accessible and unvisited border with the largest grid size as its goal. The choice of the desired border is made by maximising the utility function 24, where  $f_i^I$  and  $f_i^N$  represent the grid size of the border area and the spatial distance between the robot and the border node, respectively.  $\lambda_I$  and  $\lambda_N$  are weighting parameters associated with these two terms. Importantly, the utility function reaches its maximum value when the frontier size is large and the distance is small. This optimisation allows the robot to navigate efficiently along the shortest obstacle-free path from its current cell to the cell containing the map coordinate. As emphasised in [20], the consistent movement towards new frontiers allows the robot to extend its map into unexplored areas until the entire environment is covered.

In unstructured environments, the existing boundary selection method may become inefficient because robots tend to prioritise boundary points with high local information returns. As a result, the robot may be attracted to these points, disregarding the continuity of environmental information in the current direction of exploration. This leads to the robot revisiting previously explored locations when moving towards points with lower information returns. To address this inefficiency, this paper improves the exploration strategy by incorporating a term influenced by the direction of the exploration target point

into the utility function for profit calculation. The improved utility function  $R_d(CG_i)$  is expressed as follows

$$\begin{aligned} R_d(CG_i) &= \lambda_I \cdot f_i^I - \lambda_N \cdot f_i^N - f_i^D \\ f_i^D &= e^{\lambda_D \cdot A} \end{aligned} \quad (25)$$

where  $f_i^I$ ,  $f_i^N$  are defined the same as Eq. 24.  $f_i^D$  is an exponential function of  $A$ .  $A$  is the angle between the vectors  $\overrightarrow{T_{t-2}T_{t-1}}$  and  $\overrightarrow{T_{t-1}CG_i}$ . Similarly,  $\lambda_I$ ,  $\lambda_N$ , and  $\lambda_D$  are user-defined weightings for the size, distance and exploration direction.

4) *Stop Criteria*: The termination criterion for exploration is a critical aspect of the exploration process described above. In practical scenarios, it is often unrealistic to set a specific percentage of exploration coverage in a given area as the termination point[21]. For flying robots, efficient management of their power supply is essential due to energy constraints. It is therefore necessary to consider stopping the exploration mission either when a particular area is completed or when the exploration yield becomes relatively low. This stopping strategy is implemented to ensure that the robot can save sufficient power for a safe return. The exploration termination strategies used in this work, consist of the following two criteria:

- No further candidate exploration target points are discovered.
- The unknown area of the candidate region is below a preset threshold.

These two criteria exist side by side, and as long as either of these conditions is met, the exploration mission stops and the robot will return to the starting point.

### III. EXPERIMENTS AND DISCUSSION

#### A. Experiment setups

In real-world scenarios, we conducted experiments to validate the effectiveness of our work using the physical platform depicted in Fig. 2. Our algorithm functions within the ROS Noetic operating system. We employ a method utilizing a PD controller to steer the robot along the planned path at a frequency of 100 Hz. Simultaneously, it detects potential collisions along the path at a rate of 20 Hz, triggering a rerouting of the current trajectory in the event of a collision. The global map resolution is configured at 0.1 meters, while the dimensions of the local sensing map for path planning are set to 30m x 30m x 3m. Additionally, the obstacle point cloud's expansion radius is set to 0.5 meters. Notably, the starting point is established as the map's origin, denoted as  $x_{start} = [0, 0]^T$ . The experimental setup consists of two different scenes: a regularly maintained forest and an underground parking lot.

#### B. Evaluation on subsystems

1) *Comparison of Visual and LiDAR Odometry*: In this section, we evaluate the performance of visual and LiDAR odometry in real-world environments, as shown in Figure 7. In this experiment, we utilized the robot kit illustrated in Fig 2 (a) to conduct a comparative analysis between the visual and radar

odometry systems. Our paper implements the improved FAST-LIO as the robot's primary odometry method, concurrently running VINS-Fusion. Post-initialization, our motion planner, operated via Nomechine software's remote desktop, orchestrated the robot's autonomous flight, adhering to six pre-set waypoints. Notably, the sixth waypoint serves as the starting point  $x_{start} = [0, 0]^T$ . The outcomes are depicted in Fig. 7.

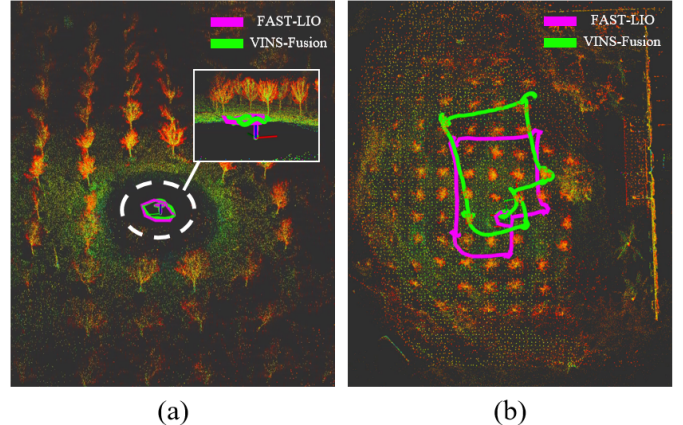


Fig. 7: Comparison of Visual and LiDAR Odometry (a) Completion of Odometry Initialization (b) Comparison of Global Paths

From Fig. 7(a), the completion of initialization showcases an excellent alignment between the FAST-LIO and VINS-Fusion odometry. However, upon completing the mission involving six waypoints, Fig. 7(b) distinctly illustrates a considerable shift in the VINS-Fusion odometry. In contrast, the LiDAR odometry remains stable, showing no significant deviation.

2) *Evaluation on Robot Motion planning*: We validate the utilised motion planning methods in the wild environments. In our experiments, we observed that the single-frame LiDAR point cloud output from the MID-360 tends to exhibit sparsity, potentially leading to certain smaller obstacles being unnoticed within the point cloud data. To address this, we amalgamated the multi-frame LiDAR point cloud data with that of the single-frame camera, presenting a comparative analysis in Fig. 8(a), (b), (c), (d). Observing 8(a) and (b), it's evident that the absence of an obstacle point cloud leads to an inadequate grid map representation, consequently rendering the planned path infeasible. However, through the fusion of 5-frame LiDAR point cloud data with single-frame camera data, depicted in Figs. 8(c) and (d), we effectively enhance our ability to perceive obstacles. The fusion of multiple sensors and frames of point cloud data addresses the challenge of perceiving smaller obstacles, enabling the motion planning process to generate feasible paths.

The motion planning for obstacle avoidance is based on optimizing paths that avoid inflated obstacles. Consequently, the choice of expansion coefficient size significantly impacts the success rate of obstacle avoidance. In Fig. 8(e),(f),(g),(h), we showcase various obstacle avoidance paths for the same scene, each utilizing different expansion coefficients. In Fig. 8(e) and (f), the depicted obstacle avoidance paths utilize an

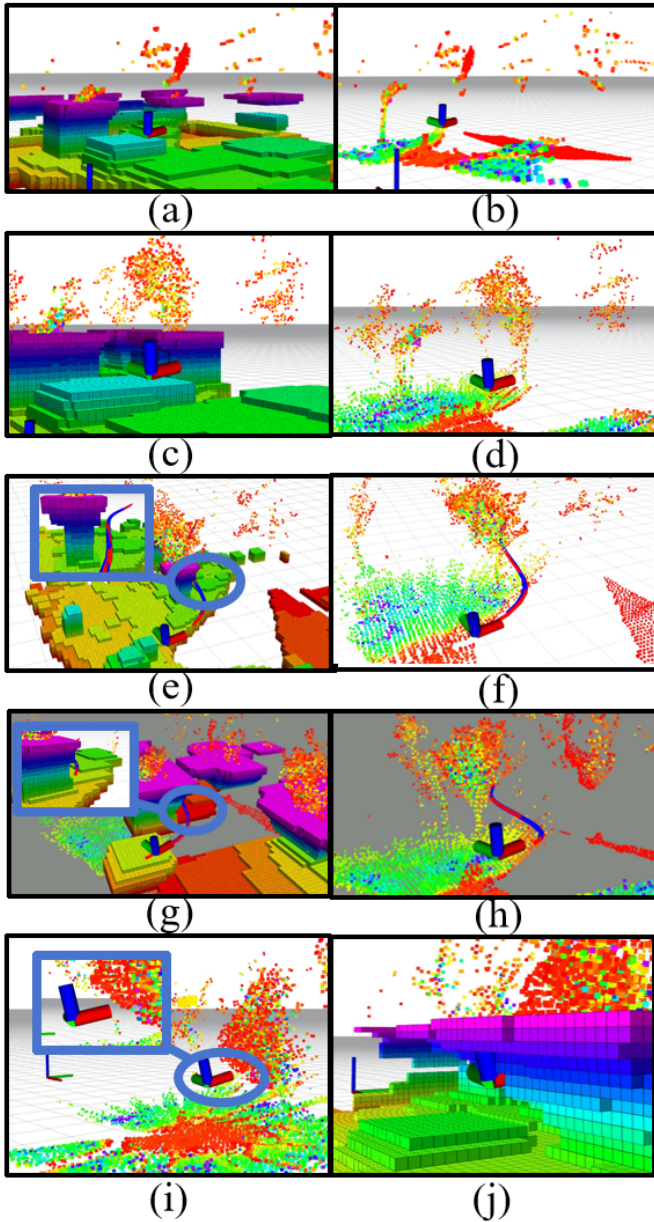


Fig. 8: Effects of Different Parameters on Motion Planning. (a) Single-frame LiDAR point cloud expansion grid map. (b) Single-frame LiDAR raw point cloud. (c) Inflation grid map corresponding to the merged point cloud. (d) Merged raw point cloud. (e) Obstacle avoidance demonstration with 0.1 inflation coefficient. (g) Obstacle avoidance with a 0.5 inflation coefficient. (f), (h) The obstacle avoidance paths of (e), and (g) in the raw point cloud. (i) robot proximity to obstacle point cloud. (j) robot within the inflated obstacle point cloud.

expansion factor of 0.1. From Fig. 8(e), it's noticeable that while these paths circumvent the expanding obstacles, they often appear excessively close to the obstacle point clouds in the original point cloud maps. Consequently, this proximity can potentially result in collisions due to the robot's size or biases within the point clouds during actual flight.

Contrastingly, in Fig. 8(g) and (h) where the paths incorporate an expansion coefficient of 0.5, Fig. 8(h) distinctly

illustrates how an increased expansion coefficient effectively maintains a safer distance between the avoidance paths and the obstacles. This augmentation notably enhances the navigability and safety of the paths. However, the expansion coefficient is not the bigger the better, too high expansion coefficient will cause the on-board computer to mistakenly think that it is in the obstacle and stop planning the path, such as Fig.8(i), (j) demonstrates the on-board computer's misjudgment in the case of expansion coefficient of 0.75.

### C. Field Experiments

To verify the feasibility and robustness of the proposed system, we conducted exploratory experiments in two different scenarios.

1) *Scene 1*: The first scenario was conducted in a forest located at South China Agricultural University in Guangzhou, Guangdong, China. The exploration process is shown in Fig. 9. According to the distribution range of the forest, we set the exploration boundaries centred on the starting point, with the farthest front/back point being 25m, and the farthest left/right point being 20m. We start the on-board computer through the remote desktop function of Nomechine to make the robot perform the autonomous exploration task. During the whole exploration process, the exploration module releases a total of six exploration target locations as shown in Fig. 9(g), which are provided with odometer information by the improved FAST-LIO in this paper, while the motion planning module used in this paper is responsible for the local path planning and optimization. It is worth noting that the sixth exploration target point is the starting point, which is due to the stopping strategy triggered by the exploration module, so the coordinates of the starting point are released as the last target point so that the robot will return to the flight path and land on its own to complete the exploration mission. A semantic processing of point cloud map based on our previous work[22], which can process object detection on point cloud in Bird-Eye-View (BEV) is utilised here to perform scene understanding in world environments, as shown in Fig. 9 (b).

2) *Scene 2*: The second scene took place in the underground parking garage of South China Agricultural University in Guangzhou, Guangdong, China, as depicted in Fig. 10 (a). Utilizing the garage entrance as our starting point, we established an exploration boundary extending 100 meters along the x-axis and 50 meters along the y-axis from the starting point. Given the initial point's orientation towards a 30-degree downhill slope, point cloud data ranging from -5.0 to -10 meters in the z-axis direction was selected as the source for the 2D Octomap map. To facilitate autonomous exploration, the onboard computer was activated using Nomechine's remote desktop function, enabling the robot to execute exploration tasks. The actual exploration route is depicted in Fig. 10 (a), while the exploration results are illustrated in 10 (b). It's important to note that due to insufficient remaining battery power for the robot to return to the starting point, remote commands were dispatched to initiate an autonomous landing upon completing the exploration mission.

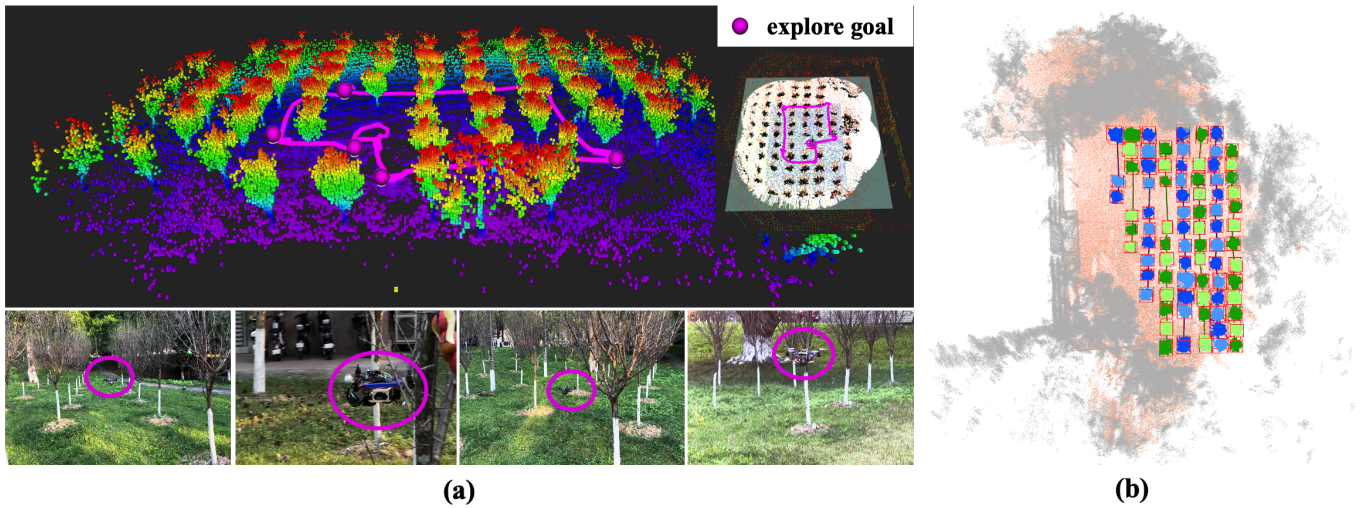


Fig. 9: Instances of an autonomous exploration mission within the forest. (a) The exploration results and on-site flight demonstration in the forest. (b) Forest semantic map based on exploration results

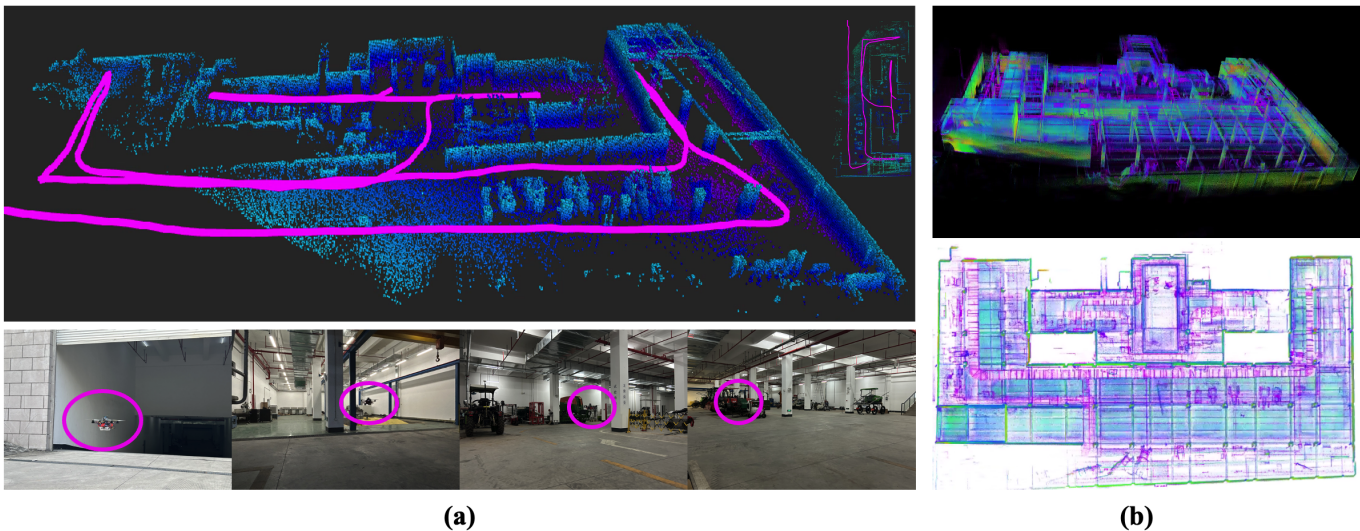


Fig. 10: Presentation of the Underground Parking Garage Exploration Process. (a) The exploration results and on-site flight demonstration in the underground parking garage. (b) Display of the Global Point Cloud Map in the Underground Parking Garage.

#### D. Failure Analysis

1) *Failure on Robot Odometry*: In our experiments, odometer failure primarily occurs in two scenarios: (1) When the fuselage lacks sufficient structural strength, the flight control IMU (Inertial Measurement Unit) receives mechanical vibrations from the motor's rotation. Consequently, the flight control system adjusts the motor based on the IMU waveform data, leading to resonance with the motor-transmitted vibration. (2) Odometer tracking failure arises during high-speed robot motion, especially when the robot undergoes rapid YAW angle changes. During exploration missions, when the target point significantly deviates from the robot's current orientation, the PD controller principle prompts the robot to perform significant spins for orientation adjustment, disabling the odometer. To mitigate this issue, the direction-focused exploration strategy proposed in this paper circumvents such

situations.

2) *Failure on Motion Planning*: This failure manifests in two scenarios:

- Being entrapped within an obstacle group causes program judgment, leading to collision and subsequent planning failure. This behaviour stems from environmental perception inaccuracies due to LiDAR point cloud sparsity and measurement errors. Notably, the obstacle point cloud's inconsistency, especially at object edges, causes sporadic jumps, resulting in the robot colliding with the obstacle cluster.
- Another prevalent failure involves obstacle avoidance. While achieving collision-free trajectories entails bypassing expanded obstacles in flight, determining an appropriate expansion coefficient in proportion to the airframe size is crucial. Excessively high expansion coefficients

exacerbate the point cloud's jumping phenomenon, leading to severe consequences.

Both issues stem from the inherent lack of accuracy in the employed environmental perception method. Addressing these challenges necessitates the development of a more precise environmental perception model.

#### IV. CONCLUSION

This paper describes the design of AREX and its autonomous exploration capabilities. The system is equipped with robust localisation, mapping and efficient exploration target selection capabilities. In particular, it prioritises continuity in exploration direction and minimises abrupt changes to increase efficiency and mitigate odometry errors. The global point cloud map generated by the exploration serves as a valuable resource for extracting semantic information about the environment. In our experiments, the real-time, high-precision environmental perception module proved to be crucial. The accuracy of environmental perception significantly influences the identification of exploration boundaries and the effectiveness of obstacle avoidance. Future efforts will focus on developing more efficient and accurate methods for perceiving and representing the environment, as well as exploring robust path-planning approaches.

#### REFERENCES

- [1] M. Grieves, "Origins of the digital twin concept," *Florida Institute of Technology*, vol. 8, 2016.
- [2] IBM. (2022) What is a Digital Twin. [Online]. Available: <https://www.ibm.com/topics/what-is-a-digital-twin>
- [3] G. M. Bisanti *et al.*, "Digital twins for aircraft maintenance and operation: A systematic literature review and an iot-enabled modular architecture," *Internet of Things*, vol. 24, p. 100991, 2023.
- [4] K. Hu, Y. Wei, Y. Pan, H. Kang, and C. Chen, "High-fidelity 3d reconstruction of plants using neural radiance field," *arXiv preprint arXiv:2311.04154*, 2023.
- [5] H. Kang and C. Chen, "Fast implementation of real-time fruit detection in apple orchards using deep learning," *Computers and Electronics in Agriculture*, vol. 168, p. 105108, 2020.
- [6] H. Kang, H. Zhou, and C. Chen, "Visual perception and modeling for autonomous apple harvesting," *IEEE Access*, vol. 8, pp. 62 151–62 163, 2020.
- [7] T. Liu, H. Kang, and C. Chen, "Orb-livox: A real-time dynamic system for fruit detection and localization," *Computers and Electronics in Agriculture*, vol. 209, p. 107834, 2023.
- [8] Z. Wang, R. Gupta, K. Han, H. Wang, A. Ganlath, N. Ammar, and P. Tiwari, "Mobility digital twin: Concept, architecture, case study, and future challenges," *IEEE Internet Things J.*, vol. 9, no. 18, p. 17452–17467, 2022. [Online]. Available: <http://dx.doi.org/10.1109/JIOT.2022.3156028>
- [9] H. Kang and X. Wang, "Semantic segmentation of fruits on multi-sensor fused data in natural orchards," *Computers and Electronics in Agriculture*, vol. 204, p. 107569, 2023.
- [10] C. Papachristos, F. Mascarich, S. Khattak, T. Dang, and K. Alexis, "Localization uncertainty-aware autonomous exploration and mapping with aerial robots using receding horizon path-planning," *Autonomous Robots*, vol. 43, pp. 2131–2161, 2019.
- [11] S. Molina, G. Cielniak, and T. Duckett, "Robotic exploration for learning human motion patterns," *IEEE Transactions on Robotics*, vol. 38, no. 2, pp. 1304–1318, 2021.
- [12] Z.-W. Hong, T.-Y. Shann, S.-Y. Su, Y.-H. Chang, T.-J. Fu, and C.-Y. Lee, "Diversity-driven exploration strategy for deep reinforcement learning," *Advances in neural information processing systems*, vol. 31, 2018.
- [13] S. Shen, N. Michael, and V. Kumar, "Stochastic differential equation-based exploration algorithm for autonomous indoor 3d exploration with a micro-aerial vehicle," *International Journal of Robotics Research*, vol. 31, no. 12, pp. 1431 – 1444, October 2012.
- [14] M. Naazare, F. G. Rosas, and D. Schulz, "Online next-best-view planner for 3d-exploration and inspection with a mobile manipulator robot," *IEEE Robotics and Automation Letters*, vol. 7, no. 2, pp. 3779–3786, 2022.
- [15] B. Lindqvist, A.-A. Agha-Mohammadi, and G. Nikolakopoulos, "Exploration-rrt: A multi-objective path planning and exploration framework for unknown and unstructured environments," in *2021 IEEE/RSJ International Conference on Intelligent Robots and Systems (IROS)*. IEEE, 2021, pp. 3429–3435.
- [16] T. Qin, S. Cao, J. Pan, P. Li, and S. Shen, "Vins-fusion: An optimization-based multi-sensor state estimator," 2019.
- [17] W. Xu and F. Zhang, "Fast-lio: A fast, robust lidar-inertial odometry package by tightly-coupled iterated kalman filter," *IEEE Robotics and Automation Letters*, vol. 6, no. 2, pp. 3317–3324, 2021.
- [18] X. Zhou, Z. Wang, H. Ye, C. Xu, and F. Gao, "Ego-planner: An esdf-free gradient-based local planner for quadrotors," *IEEE Robotics and Automation Letters*, vol. 6, no. 2, pp. 478–485, 2020.
- [19] H. Umari and S. Mukhopadhyay, "Autonomous robotic exploration based on multiple rapidly-exploring randomized trees," in *2017 IEEE/RSJ International Conference on Intelligent Robots and Systems (IROS)*. IEEE, 2017, pp. 1396–1402.
- [20] B. Yamauchi, "A frontier-based approach for autonomous exploration," in *Proceedings 1997 IEEE International Symposium on Computational Intelligence in Robotics and Automation CIRA'97: Towards New Computational Principles for Robotics and Automation*. IEEE, 1997, pp. 146–151.
- [21] G. Amorín, F. Benavides, and E. Grmapin, "A novel stop criterion to support efficient multi-robot mapping," in *2019 Latin American Robotics Symposium (LARS), 2019 Brazilian Symposium on Robotics (SBR) and 2019 Workshop on Robotics in Education (WRE)*. IEEE, 2019, pp. 369–374.
- [22] Y. Pan, H. Cao, K. Hu, H. Kang, and X. Wang, "A novel perception and semantic mapping method for robot autonomy in orchards," *arXiv e-prints*, pp. arXiv-2308, 2023.